SOFT ROBOTS

Upgrading and extending the life cycle of soft robots with in situ free-form liquid three-dimensional printing

Elgar Kanhere[1], Théo Calais[2], Snehal Jain[1], Aby Raj Plamootil Mathai[3], Aaron Chooi[3], Thileepan Stalin[3], Vincent Sebastian Joseph[1], Pablo Valdivia y Alvarado[1,3,4]*

Soft robotics hardware, with numerous applications ranging from health care to exploration of unstructured environments, suffers from limited life cycles, which lead to waste generation and poor sustainability. Soft robots combine soft or hybrid components via complex assembly and disassembly workflows, which complicate the repair of broken components, hinder upgradability, and ultimately reduce their life spans. In this work, an advanced extrusion-based additive manufacturing process, in situ free-form liquid three-dimensional printing (iFL3DP), was developed to facilitate functional upgrades and repairs in soft robots. A yield-stress hydrogel—a type of material that can maintain its shape until sufficient stress is applied—was first printed directly onto the robot surface, serving as a support for printing new components. This technique enabled the fabrication of advanced components with seamless integration onto already assembled robots. These components could combine multiple materials with intricate geometries, including overhangs and high–aspect ratio shapes, that are considerably challenging to manufacture and integrate via traditional methods such as casting. This approach was successfully applied to upgrade an existing soft robot by adding three advanced functionalities: whisker-like sensors for tactile feedback, a grasping mechanism, and a multifunctional passive whisker array. This study showcases the easy repairability of features, new and old, substantially extending the robot's life span. This workflow has potential to enhance the sustainable development of soft robots.

INTRODUCTION

Soft robotics, a rapidly evolving field in robotics research, is characterized by its incorporation of soft and compliant materials into novel robotic frameworks. Such integration has led to considerable advancements in terms of functionality, actuation, and robustness (*1*, *2*), finding applications across various sectors, from health care and wearables (*3*, *4*) to exploration in unstructured environments (*5*–*7*) and tasks in human-centric contexts (*8*–*10*). As soft robotics technologies become more prevalent in daily applications, an emphasis on sustainability and life cycle management is increasingly pertinent (*11*, *12*).

Although there is substantial research on materials sourced from renewable resources (*13*–*15*), the domain of life cycle management in soft robotics remains underexplored. This can be attributed to the relatively early stage of development in this field, with a prevailing focus on developing new materials, sensors, actuators, and control mechanisms (*16*). Furthermore, the inherent complexity of soft robots, which combine soft bodies with rigid components like motors and electronic systems (*6*, *17*–*20*), presents a challenge for easy assembly, disassembly, and, consequently, repairs (*21*, *22*).

Preliminary approaches in this domain have considered modularity as a means to simplify rearrangements and repairs (*23*–*26*) and research into efficient and cost-effective methods for recycling prevailing nonbiodegradable materials, such as room-temperature vulcanized (RTV) silicones (*27*). Another promising strategy is the postproduction enhancement of capabilities, a concept previously investigated in electronic device domains (*28*–*30*). Although promising, this approach requires rethinking the manufacturing process to seamlessly incorporate diverse components across the lifetime of the product (*28*). Developing more integrated workflows facilitating the incorporation of additional capabilities could substantially contribute to development of this approach.

Additive manufacturing (AM) has emerged as a potential solution to reduce environmental footprint (*31*–*33*), offering benefits such as minimized waste, optimized material use, and decentralized production (*33*). However, despite a large range of AM technologies, the lack of compatibility between different AM technologies and the limited range of processable materials per technology still limit broad influence (*34*), explaining why AM adoption in soft robots is still in its infancy (*35*, *36*).

Recent advances in AM, such as direct ink writing (DIW) (*37*), embedded three-dimensional printing (e3DP) (*19*, *38*), or free-form liquid 3D printing (FL3DP) (*39*–*41*), have shown promise in manufacturing functional multimaterial structures. Specifically, FL3DP has notably widened the range of processable materials and printable geometries (*39*–*41*). The use of a yield-stress gel as temporary support enables the extrusion of inks with low viscosities or long solidification kinetics as well as the manufacture of overhangs or high–aspect ratio structures and enhances the robustness of multimaterial components (*40*). However, in the current approach, the gel is placed in a container in which objects can be printed, thus limiting the available workspace.

In this study, the printability of the support gel by DIW was explored and leveraged to enable the local deposition of a custom gel volume, where needed, followed by the FL3DP of functional soft components within. This strategy, called "in situ FL3DP" (iFL3DP), was explored to upgrade the functionalities of an existing soft robot by printing advanced functional components directly on the old robot's surface. The aim of the present work is twofold: to expand the capabilities of an old robot through the seamless integration of

[1]Digital Manufacturing and Design Centre (DManD), Singapore University of Technology and Design, Singapore, Singapore. [2]ICB UMR 6303 CNRS, Belfort-Montbéliard University of Technology, UTBM, Belfort, France. [3]Engineering Product Development (EPD), Singapore University of Technology and Design, Singapore, Singapore. [4]Singapore-HUJ Alliance for Research and Enterprise (SHARE), Smart Grippers for Soft Robotics (SGSR) Programme, Campus for Research Excellence and Technological Enterprise (CREATE), Singapore 138602, Singapore.
*Corresponding author. Email: pablov@sutd.edu.sg

additional capabilities and to prolong the useful robot life span by facilitating component upgrades and repairs. To illustrate the possibilities enabled by iFL3DP, we used a batoid-inspired underactuated swimming robot developed in previous studies (*19*, *42*) as a test bed. The first generation was able to swim autonomously using preprogrammed flapper actuation but lacked onboard sensors, which hindered any type of closed-loop control. As a result, the integration of three additional and essential components was explored: tactile sensing via long whiskers for obstacle detection and texture sensing, actuated hooks to carry payloads and perch on docking platforms, and passive thermal sensing and sample collection via an array of short whiskers. These functionalities were chosen because they offer a distinct improvement of the robot's capabilities regarding environment interactions and require intricate geometries with multimaterial structures that are challenging to manufacture using traditional casting methods. The components were added directly on the skin of the old robot via iFL3DP, resulting in strong and robust adhesion. The modularity of these additions enabled easy repairs or replacements of damaged components, thus further prolonging the life span of the robot. Overall, these results illustrate the capability of iFL3DP to facilitate the integration of advanced components on existing devices, upgrade existing capabilities, and contribute to the sustainable development of soft robots.

RESULTS

iFL3DP

The use of iFL3DP for upgrading or repairing soft robotic devices is illustrated in Fig. 1A, where two scenarios are highlighted. First, for an already in-use "generation 1" robot, iFL3DP enables integration of multimaterial components directly on the robot's skin, even on uneven surfaces (see Fig. 1A). This approach is applicable for

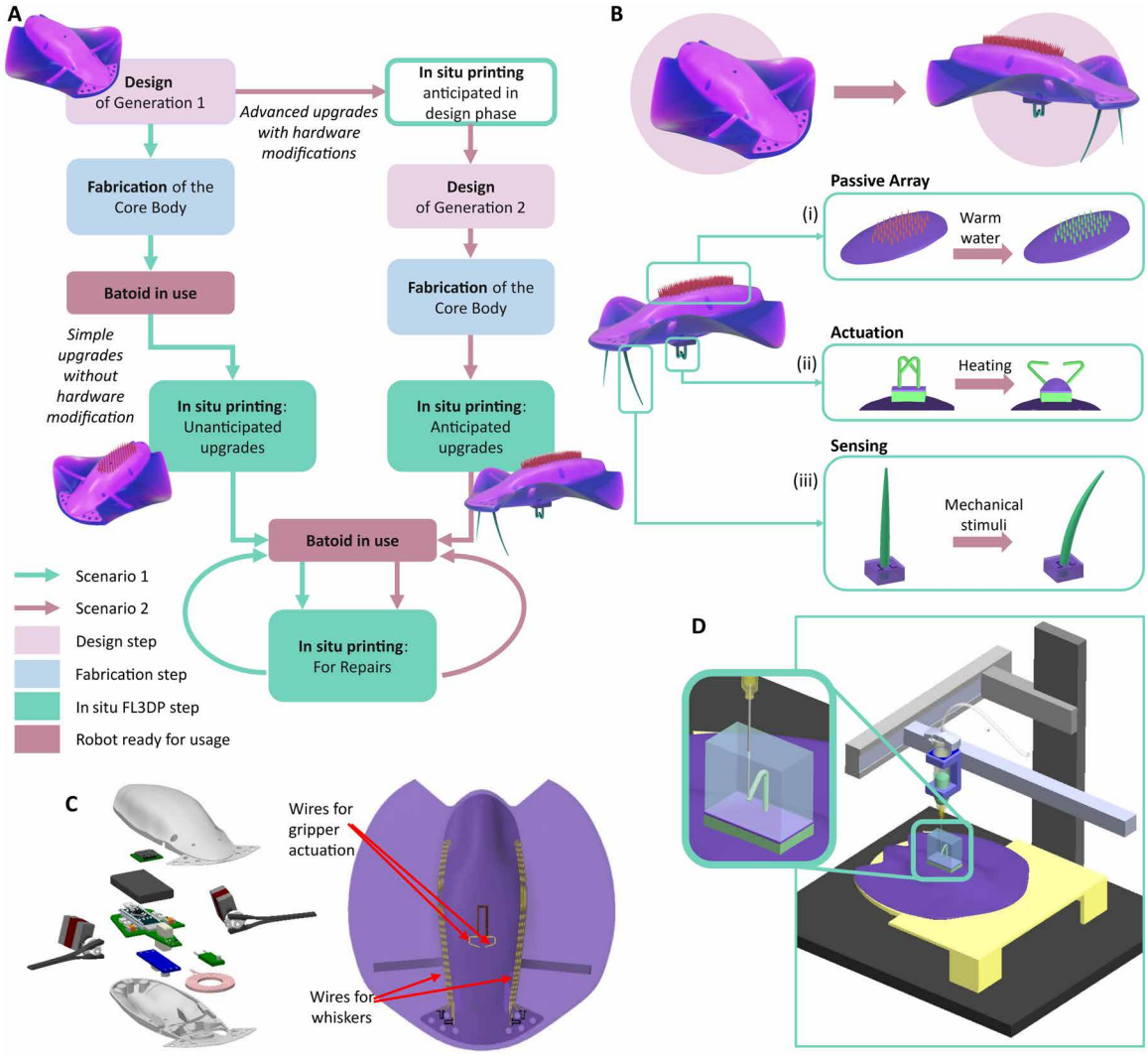

Fig. 1. Upgrading and life extension of soft robots. (**A**) Workflow chart showing how iFL3DP can be used for upgrades and repairs during the robot's life span through two scenarios. (**B**) Upgrading a soft batoid-like swimming robot through the addition of (i) passive temperature sensing, (ii) actuated hooks for perching and payload carrying, and (iii) tactile sensors for obstacle detection and seafloor bathymetry analysis. (**C**) Illustration of the internal structure of the batoid-like robot and the hardware modifications required from a generation 1 design to enable electrical connections for new components. (**D**) Illustration of the iFL3DP process to enable fabrication and direct integration of additional components.

upgrading robots already manufactured, on the condition that these upgrades are compatible with the existing robot's hardware (for example, generation 1 electrical circuits or power systems).

Incorporating more advanced upgrades taking advantage of iFL3DP can be envisioned during the product development phase, before the robot's fabrication. In this second scenario (see Fig. 1A), a generation 2 robot's design can be iterated from a generation 1 robot to accommodate more advanced hardware modifications, such as new electrical connections or computing capabilities required for actuation and sensing. The generation 2 robot can then be fabricated using iFL3DP to integrate additional functionalities anticipated in the design phase by printing multimaterial components with intricate geometries directly on the robot's skin. Furthermore, iFL3DP facilitates repairs of any component susceptible to wear and tear once the robot is deployed and in use, given that the damaged component can be easily reprinted on the robot. iFL3DP considerably reduces the volume of support needed compared with traditional FL3DP, without posing substantial restrictions on working space or increasing postprocessing time. Regarding postprocessing, a simple wash-off with a gentle flow of water enables cleaning of the components in a couple of minutes (see movie S1) given that the hydrogel does not interact with the polymerization of the elastomer.

A batoid-like soft robot introduced in earlier studies (*19*, *42*) was used to explore both scenarios. Starting from a generation 1 foundational design—the original robot—limited to preprogrammed autonomous swimming, the objective was to enhance the capabilities of the robot through the addition of three key components illustrated in Fig. 1B, with a distinct emphasis on repairability. For the first component, illustrating the first scenario, a temperature-sensitive array of whiskers was added on the curved dorsal area of the robot [Fig. 1B (i)]. The array was composed of a dense distribution of high–aspect ratio whiskers serving a dual purpose: to collect biological samples captured by the array and to function as a temperature indicator detectable by external devices. This design was chosen to illustrate the capability to integrate high–aspect ratio structures in a straightforward manner, even on curved surfaces, using iFL3DP. Being entirely passive, this addition did not require any electronics or power modifications and was instantly operational after printing on the generation 1 robot.

The subsequent components illustrated the second scenario. First, a pair of thermally actuated hooks, situated on the robot's ventral region, was fabricated to enable low-power tasks, such as docking and payload carrying [Fig. 1B (ii)]. Two hook-like whiskers were printed on a soft membrane placed on top of a chamber filled with a low–boiling point liquid. The liquid volume change, controlled by joule heating of a nichrome wire, led to the deformation of the membrane and opening of the hooks. The third component consisted of two catfish barbel–like whiskers mounted on resistive sensors, strategically positioned on the frontal part of the robot [Fig. 1B (iii)]. The primary function of these whiskers was to enable tactile feedback, facilitating obstacle avoidance and seabed texture analysis.

As illustrated in Fig. 1C, these two components required internal hardware modifications to the generation 1 robot, including modifications of the onboard electronics and the installation of electrical connections for both joule heating and sensing. This led to the development of a generation 2 batoid robot, which was then used as a robotic base on which the three new components were integrated using iFL3DP. More information on the modifications to the internal robotic system is provided in fig. S1, and the new functionalities provided by the additional features are listed in table S1. It should be noted that the components' multimaterial composition, which blended elastomers of varying moduli, liquids, conductive wires, and intricate geometries on uneven surfaces, would pose substantial challenges to conventional soft robotics manufacturing methods such as casting or molding, as illustrated in fig. S2.

Once designed, the components could be 3D printed directly on the robot's surface using iFL3DP, streamlining the integration process by minimizing manufacturing steps, such as separate fabrication of sensors, assembly, and integration steps. As illustrated in Fig. 1D, the required volume of gel was deposited on the surface, followed by extrusion of the inks. This characteristic enables a drastic decrease in the support gel volume required compared with traditional FL3DP, where robots or components would typically be fully immersed in the support gel. Here, a nanoclay-based hydrogel similar to the one reported in (*40*) was used as a support (5 wt % Laponite XLG dispersed in deionized water; see Materials and Methods). Furthermore, these hydrogels do not cause environmental harm.

Robotic platform design

The batoid robot used in this study had a design similar to the one described in (*19*) and (*42*). Briefly, two fins made of soft silicone rubber (Ecoflex 00-30, Smooth-On, noted EF30) were actuated by two lepidotrichia-inspired flappers (*43*) linked to servomotors, which were controlled by an onboard microcontroller (*42*). The robot's speed and heading depended on the preprogrammed flapping frequency and amplitude of each fin, with instructions relayed via wireless Bluetooth communication. The robot was designed to be neutrally buoyant, with all electronic components enclosed in a thermoplastic hull. This hull was encapsulated by an elastomeric skin to guarantee waterproofing (for details, refer to Materials and Methods and fig. S1).

Fabrication process of the thermochromic whisker array

Figure 2 shows the workflow to fabricate each component via iFL3DP. Geometry details of the various new whisker features are shown in Fig. 2A. A schematic view of the batoid robot with three new components is shown in Fig. 2B, with the associated manufacturing sequence shown in Fig. 2 (C to E). A thermochromic whisker array was added to the robot's dorsal area. This array was composed of 38 whiskers, arranged in five rows, each standing at a 12-mm height with a base diameter of 2 mm [Fig. 2A (i)]. These dimensions, ~25% of the robot's height, were chosen to illustrate the manufacturing of high–aspect ratio whiskers while also limiting drag. The whiskers were made of a stiff silicone (Smooth-Sil 960, noted SS960, elastic modulus $E_{100\%} = 1.9$ MPa) mixed with thermochromic pigments (Hali thermochromic pigment) set to transition from red to green when the external temperature exceeds 31°C.

The fabrication sequence for the thermochromic whisker array is shown in Fig. 2C and movie S1. The first step involved the conformal printing of a thin layer of EF30 onto the robot's middorsal region (for a detailed methodology on conformal printing atop curved interfaces, refer to fig. S3). This layer served as an anchoring adhesive to secure the whiskers to the old robot's skin. More information on the adhesion strength of printed layers cured on elastomeric bases can be found in the "T peel test" section of Supplementary Text (see fig. S4). The support gel was then printed on the surface (total height of ~20 mm), followed by extrusion of the whiskers. After curing

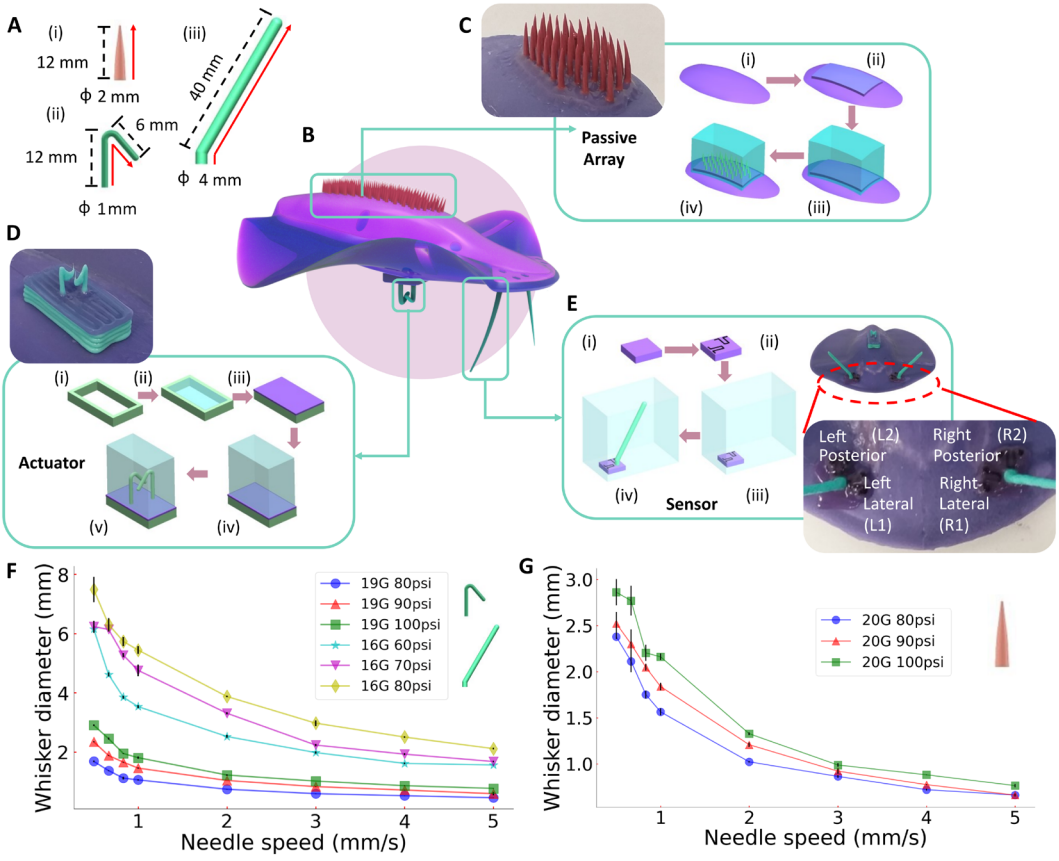

Fig. 2. iFL3DP workflow for three new functional components. (**A**) Geometrical parameters of (i) thermochromic whiskers, (ii) hook-like whiskers, and (iii) tactile whisker sensors. Red arrows show the needle paths during printing. (**B**) Schematic of batoid with three new functional components. (**C**) Fabrication steps for the thermochromic whisker array: (i) dorsal area of the batoid, (ii) DIW of an Ecoflex 00-30 (EF30) layer serving as a graft layer, (iii) DIW of the support hydrogel on top of the graft layer, and (iv) FL3DP of whiskers. (**D**) Fabrication of the hook-like whisker actuators: (i) DIW of Smooth-Sil 960 (SS960) cavity walls, (ii) DIW of the support hydrogel, (iii) DIW of a cavity top EF30 layer, (iv) DIW of the support hydrogel, and (v) FL3DP of SS960 hooks. (**E**) Fabrication of the tactile whisker sensors: (i) DIW of an EF30 layer, (ii) e3DP of the carbon grease strain gauge, (iii) DIW of the support hydrogel, and (iv) FL3DP of SS960 whiskers. (**F**) Effect of printing parameters on whisker dimensions (tactile whisker sensor and hook-like whisker); 16- and 19-G needles have inner diameters of 1.35 and 0.81 mm, respectively. The error bars in the graph denote the SD from three readings taken along the length of the whiskers. (**G**) Effect of printing parameters on whisker dimensions (thermochromic whisker); a 20-G needle has an internal diameter of 0.66 mm. The error bars in the graph denote the SD from three readings taken along the length of the whiskers.

(typically ~16 hours at room temperature or ~2 hours at 60°C), the support was washed off.

Fabrication process of the hook-like whisker actuator

The actuator design incorporated two hook-like whiskers, each measuring 12 mm in height and 1 mm in diameter and made from stiff SS960 to provide enough mechanical resistance [see Fig. 2A (ii)]. Like for the thermochromic array, these dimensions were chosen to limit the increase in the robot envelope while providing enough length to carry payloads or to dock on landing platforms. The whiskers were anchored on a soft membrane positioned atop an ~2.4-ml cavity. The whiskers' aperture was controlled by changing the temperature of a low–boiling point liquid (Novec 71IPA engineering fluid, boiling temperature of 54°C) via joule heating of a nichrome wire connected to the robot's battery and controlled by a double latch relay (Omron G6SK-2; see fig. S5).

The iFL3DP process of the hook-like whisker actuator is shown in Fig. 2D and movie S2. First, a 20-cm-long nichrome wire was coiled inside the old robot's ventral region to provide optimal contact surface area with the liquid. Although the wire was placed manually for the robot presented in this study, automation of the wire placement was also demonstrated using automated fiber embedding technology (*44*) and is reported in fig. S6. Next, SS960 was printed via DIW to form the cavity walls enveloping the nichrome wire, with dimensions of 34 mm by 14 mm by 5 mm (length, width, and height, respectively) [see Fig. 2D (i)]. The hydrogel was then printed via DIW to fill up the cavity, followed by the printing of a 1-mm-thick membrane of EF30 on top of the cavity via DIW. Next, an ~15-mm-height support hydrogel was extruded on top of the membrane [Fig. 2D (iv)], followed by extrusion of the two hook whiskers via FL3DP. After curing, the support hydrogel was washed off, and the cavity was drained and filled with the low–boiling point liquid using a syringe. The use of the low–boiling point fluid as a support hydrogel was not possible without affecting the phase-change property of the liquid, contrary to a previous work where a functional dielectric liquid could be modified to be used as a support for the FL3DP of hydraulically enhanced dielectric elastomer actuators (*41*).

Fabrication process of the tactile whisker sensors

Tactile capabilities were introduced through the integration of two obliquely positioned whiskers on both the left and right flanks of the robot's anterior ventral section, as illustrated in Fig. 2E. The whiskers were 40 mm long, corresponding to ~20% of the robot's total body length, similar to the Japanese goatfish (*45*). This length was chosen to provide enough clearance from the ventral region (~25 mm) to feel seabed textures without crashing against them and to only detect close obstacles. The whiskers were made of stiff SS960 to better transfer mechanical stimuli felt on the whiskers to the strain gauges located at their bases. The dynamic responses of these whiskers were registered by two strain sensors located at the base of each whisker (carbon grease–based strain gauges). The location of these sensors, labeled L1 and L2 for the left lateral and left posterior and R1 and R2 for the right lateral and right posterior, is shown in Fig. 2E. Each sensor interfaced with the robot's internal electronic framework via wires running parallel to the robot's central axis (see Fig. 1C). Whisker movements triggered resistance changes in the embedded sensors, which led to voltage changes that were recorded on an onboard secure digital (SD) card (see fig. S1).

The four steps of the iFL3DP workflow are illustrated in Fig. 2E and movie S3. First, an EF30 layer was printed on the robot's surface, setting the stage for whisker integration. Next, the strain sensors were embed–3D printed in the freshly printed layer using carbon grease. These sensors were connected to the robot's circuitry via wire contacts incorporated into the robot skin. A support hydrogel was then printed on top of the uncured EF30 layer, reaching a height of ~50 mm with an approximate volume of 75 cm^3. Last, the whiskers made of SS960 were fabricated via FL3DP with a 30° angle. After curing, the support was washed off, and the whisker sensors were operational.

iFL3DP of high–aspect ratio whisker-like structures

Central to iFL3DP was the initial printing of a yield-stress hydrogel. This gel's rheological properties inherently allowed for DIW: Flowing like a liquid during extrusion, the gel solidified instantly at rest once extruded. Laponite-based hydrogels were chosen in this study because of their ease of preparation and rapid transition between gel and liquid states (*40*). An in-depth investigation of the influence of Laponite concentration on rheological properties and printability is provided in the "Rheological properties and printability of the support bath" section of Supplementary Text. A strong correlation between the composition of the gel and its stability against gravity was observed. Printed rectangular volumes with aspect ratios of up to 2.5 were reachable at a 6 wt % concentration. For the remainder of the study, support hydrogels with a 5 wt % concentration were used.

Before the iFL3DP of whiskers, a fresh thin layer of silicone rubber was extruded on the robot's skin to be used as a graft to bond whiskers to the skin. The support hydrogel was then extruded onto the desired section of the robot's surface to enable iFL3DP of the whiskers. Various customizations of features, achievable by tweaking the needle trajectory, speed, and input pressure, can easily be explored with iFL3DP. Here, the whisker printing process comprised three main phases: A slower extrusion speed was used to ensure a robust thicker base embedded in the anchoring layer; a uniform speed was then adopted to maintain consistent whisker thickness; and extrusion stopped while needle motion continued, leading to the formation of a tapering whisker tip.

Two elastomeric inks were used: a pure SS960 formulation for the tactile whisker sensors and hook-like whiskers and a variant of SS960 mixed with thermochromic pigments specifically for the thermochromic whiskers (see Materials and Methods for compositions). The incorporation of thermochromic pigments modified the rheological characteristics of the SS960 ink. Consequently, the effects of different printing parameters on the whisker's diameter for both ink formulations were explored. The findings are shown in Fig. 2 (F and G) and detailed in the "Rheological properties and printability of the inks" section of Supplementary Text, along with a characterization of the minimum resolution achievable. On the basis of these outcomes, the optimal extrusion speed and needle diameter were selected and detailed in Materials and Methods.

Characterization of the tactile whisker sensors

The strain gauges were first characterized using both dynamic and static whisker experiments. As shown in Fig. 3A, the robot was positioned inside a water tank, and a 2-mm-diameter rod was moved horizontally to contact the whisker. The resulting voltage changes for each strain gauge (due to changes in resistance) were recorded using a digital multimeter (Keithley DMM 6500). The rod's speed and displacement were controlled using a linear stage (Zaber X-BLQ1045-E01).

The dynamic behavior of the strain gauge was investigated by exciting the whisker at its midpoint to induce a 10-mm displacement at 50 mm s^{-1}. This procedure was repeated over 100 cycles, with the relative change in resistance ($\Delta R/R_0$) for the left posterior (L2) gauge plotted in Fig. 3B. The graph showed a consistent sensor response across 100 cycles. Each rod contact resulted in a pronounced resistance surge (see close-up in inset), averaging 0.060 ± 0.014. The correlation between impact velocity and $\Delta R/R_0$ was further investigated and is reported in fig. S9. Increasing speeds led to larger amplitude changes from ~0.03 to ~0.075 but stabilized beyond 50 mm s^{-1} [~0.3 body lengths (BL) s^{-1}].

The strain gauge's response to static stimuli was also investigated. The whisker was similarly excited at its midpoint, inducing a 10-mm displacement at 50 mm s^{-1}, but the rod remained in position for 30 s. The $\Delta R/R_0$ for both L1 and L2 sensors during a single impact is plotted in Fig. 3C. Both gauges registered resistance spikes during the stimulus's onset and cessation. Over the 30-s duration, the posterior gauge decreased beneath the baseline, whereas the lateral gauge stabilized above the baseline, suggesting that the posterior gauge compressed as the lateral gauge extended. This static cyclic behavior was repeated over 25 cycles and was found to be consistently repeatable (see fig. S9).

Last, sensor responses during the robot's swimming motions were evaluated to establish baseline patterns caused by the fin flapping. Free swimming experiments were conducted in water at varying speeds of 0.1, 0.2, and 0.4 BL s^{-1} (for a 40° flapping amplitude and frequencies of 0.5, 1.0, and 1.5 Hz, respectively). The output voltages for the left whisker sensors (L1 and L2) were recorded by the microcontroller, stored on an onboard SD card, and collected via wireless Bluetooth. The voltages for the three frequencies are reported as a function of time in Fig. 3D. Discernible voltage peaks, synchronized with the flapping frequency, confirmed the effective capture of fin movements. The posterior gauge registered a higher output, likely because of its proximity to the flapper (as seen in Fig. 2E). Comparable patterns were also noted in air. These observations

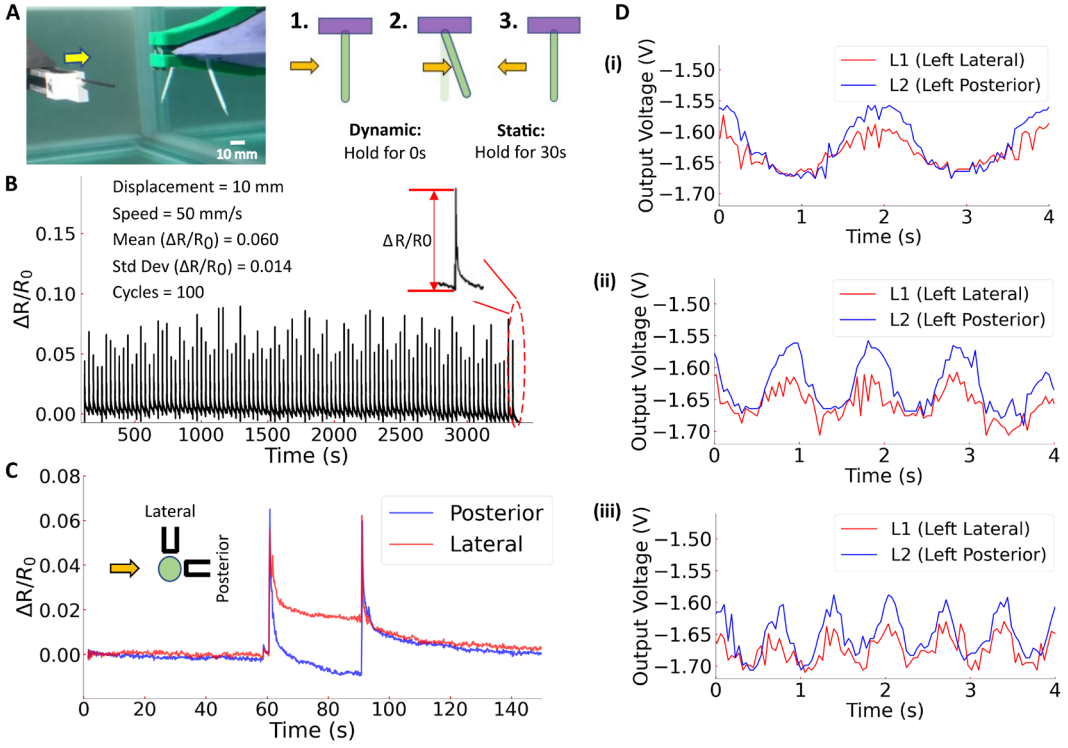

Fig. 3. Tactile whisker sensor characterization. (**A**) Experimental setup for the characterization of the strain gauges. The horizontal motions of a 2-mm-diameter steel rod were controlled to excite the whiskers in both dynamic and static experiments. Scale bar, 10 mm. (**B**) Resistance changes on the posterior left gauge due to dynamic cyclic loading. The average and SD in ($\Delta R/R_0$) were calculated from 100 cycles. (**C**) Resistance changes on the posterior and lateral left gauges due to static cyclic loading. (**D**) Output voltage of both lateral and posterior left gauges during robot free swimming at (i) 0.5 Hz, (ii) 1.0 Hz, and (iii) 1.5 Hz.

are detailed and reported in fig. S9, along with the characterization of the repeatability of signal sensor.

Whisker sensor applications

Obstacle detection

The reliability of the sensor signals facilitated the detection of various mechanical stimuli, such as unanticipated obstacles, prompting the robot to maneuver away from the obstacle. An algorithm was used to identify deviations in sensor outputs beyond a designated threshold when compared against a moving average. If identified, then the algorithm marked the deviation as a peak (*46*) and initiated a predetermined behavior, thus enabling obstacle detection and avoidance (see Fig. 4, A to C, and Materials and Methods).

The robot's new obstacle detection capabilities were evaluated during free swimming experiments using custom-made obstructions. A state machine behavior, detailed in Fig. 4A, was defined as follows: The robot's default state was to swim rectilinearly flapping both fins at 1 Hz with the same amplitude; if an anomaly was registered on the left whisker, then the robot's state changed to a rightward movement by deactivating the right fin and accelerating the left fin flapping to 1.5 Hz; after a preset duration of 4 s, the robot state switched back to linear motion using original settings of 1 Hz for both fins.

Movie S4 shows the robot's ability to detect and avoid an obstacle. Figure 4B shows snapshots of the various states. The output voltages versus time from all four strain gauges are shown in Fig. 4C. The left whisker contact with the object at time t_1 was identified, inducing sharp variations in L1 and L2 outputs, triggering the algorithm to modify the flapping frequencies. The flapping frequencies before t_1, after t_2 (the time at which the linear movement resumes), and between t_1 and t_2 were reflected in the voltage output of each gauge.

Bathymetry

Bathymetry feedback, or the ability to identify various seabed topologies, is useful in underwater navigation, in particular when topology maps already exist. A simulated seabed comprising three zones with pebbles of different dimensions was used for the experiments: white cobbles with average diameters of 100 to 120 mm, black coarse gravel with average diameters of 20 to 40 mm, and red-white fine gravel with average diameters of 6 to 8 mm (*47*). The upgraded robot was attached to a linear stage (Zaber X-BLQ1045-E01) and towed at a steady speed of 10 mm s^{-1} over the simulated seabed surface at an elevation that allowed contact between the tactile whiskers and the pebbles (see Fig. 4D and movie S5). Outputs from L2 and R2, shown in Fig. 4E, exhibited sharp fluctuations at distinct frequencies corresponding to the varying pebble sizes. The intervals between these voltage fluctuations could be used to infer the size range of the pebbles. For instance, in Fig 4E, intervals of 11, 2.5, and 0.9 s at a moving speed of 10 mm s^{-1} equated to distances of 110, 25, and 9 mm, respectively, mirroring the size brackets of the respective pebble categories.

These variations were characteristic of the whisker's stick-slip dynamics: The whisker entered in contact with a pebble, clung briefly (causing a gradual voltage increase), and then detached, soon touching the next pebble (causing a sharp voltage drop). Such tactile events mimic those used by insects and mammals to discern textures (*48*) and were further analyzed on regulated textures (see fig. S9).

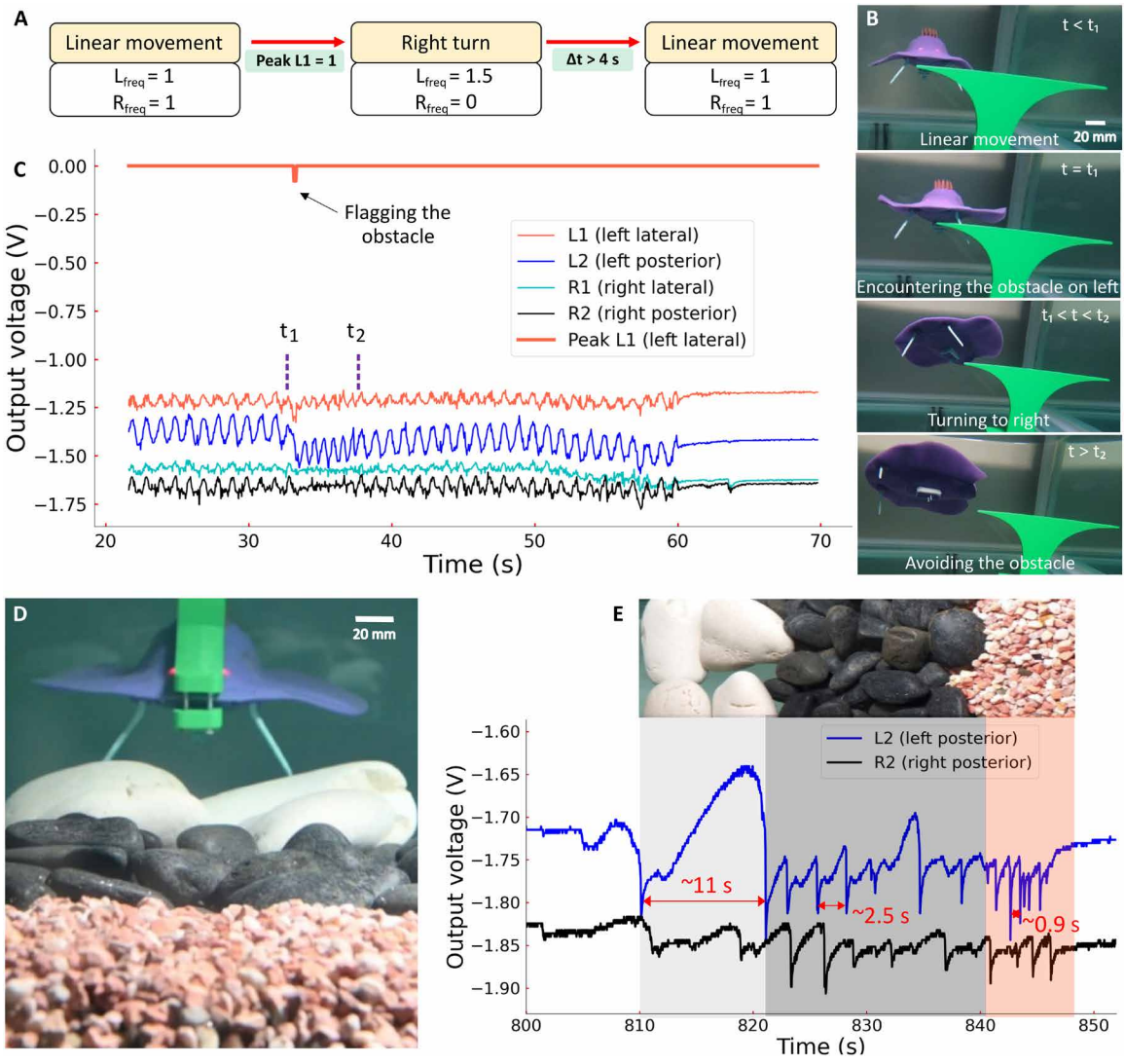

Fig. 4. Whisker sensor applications. (**A**) State machine diagram for obstacle detection and avoidance behavior. (**B**) Snapshots from movie S4 illustrating the sequence of events during obstacle detection. Scale bar, 20 mm. (**C**) Voltage outputs from the four strain gauges during obstacle detection. (**D**) Front view of a batoid-like robot being towed over the artificial seafloor made of different pebble sizes. Scale bar, 20 mm. (**E**) Voltage outputs of the posterior sensors during surface scan.

Additional runs conducted for bathymetry and obstacle detection can be seen in fig. S10.

Hook-like whisker actuator

Characterization

Finite element analysis (FEA) was first conducted using Abaqus to refine the design features of the chamber and the hook-like whiskers (see Fig. 5A). A chamber with dimensions of 10 mm by 7 mm by 5 mm was filled with a low–boiling point liquid. For simplification purposes, a smaller chamber was used to limit computation time, and ethanol was chosen as a liquid model because density and volumetric temperature coefficients are well documented. Two hook-like whiskers were positioned on the top membrane (see Fig. 2A for dimensions). The cavity walls and the two whiskers were modeled using SS960 properties, and the soft top membrane was modeled using EF30 properties. Both materials were modeled as neo-Hookean hyperelastic materials (see Materials and Methods for more details). The simulation was conducted by changing the temperature of the internal fluid from 25 to 90°C, resulting in membrane deformation leading to the opening of the whiskers (see Fig. 5A). The FEA studies qualitatively matched experimental observations and confirmed the suitability of the geometric design choices.

A series of experiments was then conducted to correlate the heating capacity of the nichrome wire with actuation time. With the current being fixed by the battery (0.35 A at 4.20 V), the heating was controlled by on/off cycles. The effect of actuation duration on the opening angle of the hook-like whiskers was then assessed by applying 5-s on/1-s off cycles on the nichrome wire and recording the deformation of the membrane (see fig. S11 for more information). As seen in Fig. 5B, an angle of 51° was achieved in a span of 60 s.

Application: Perching

The hook-like whiskers allowed the upgraded robot to land on a designated perching site (see movie S6). A sequential breakdown is shown in Fig. 5C, where the robot approached and anchored to a

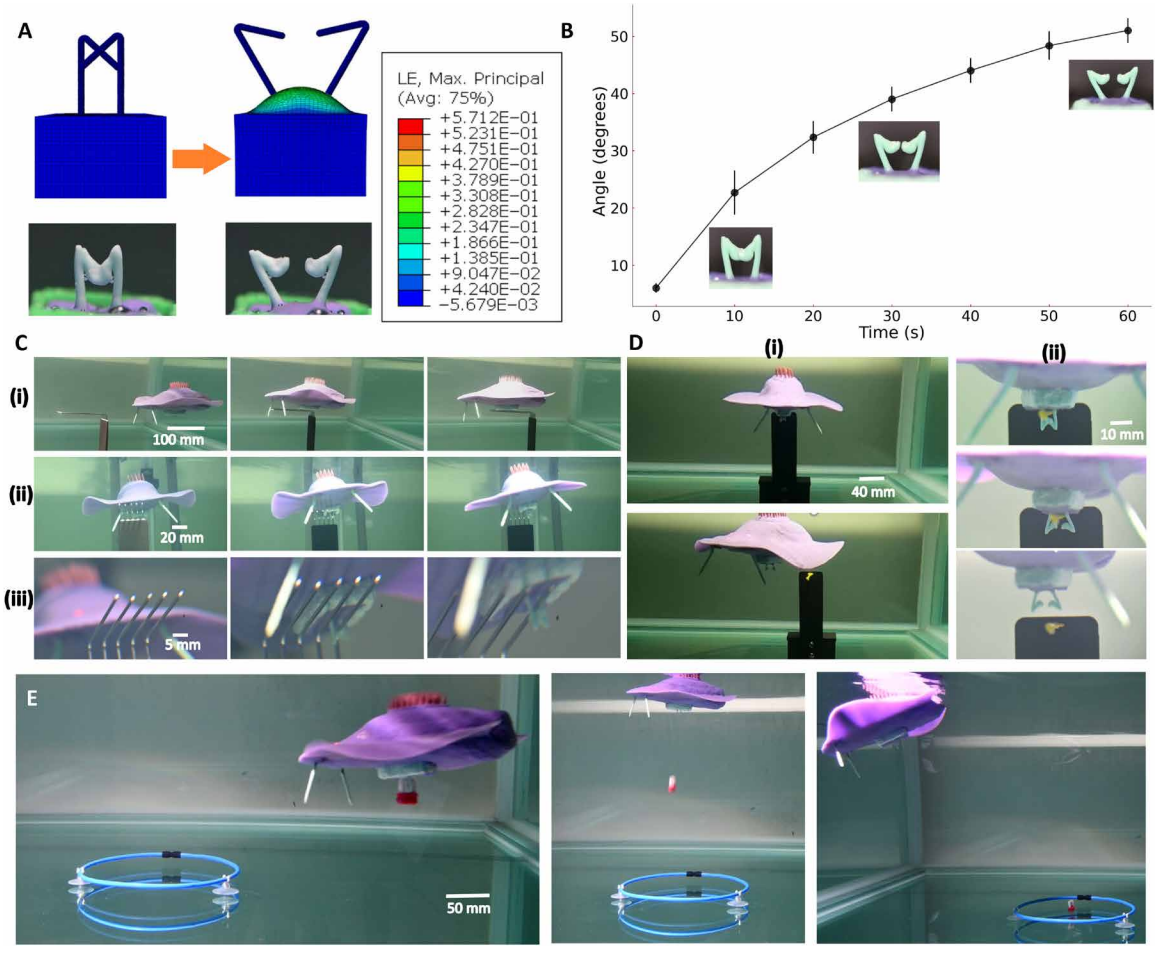

Fig. 5. Hook-like whisker actuator. (**A**) FEA of the membrane deformation when heating at 90°C an ethanol-like liquid placed within the cavity. Membrane deformations lead to the opening of the hook-like whiskers. The results match well with the experimental observations shown in the images below. (**B**) Plot showing the increase in hook-like whisker opening angle versus actuation time. The error bars denote the SD over three runs. (**C**) Sequence of events during landing on a perching site: (i) global side view, (ii) global front view, and (iii) close-up view. Scale bars, 100, 20, and 5 mm, respectively. (**D**) Sequence of events showing the upgraded robot taking off from the perching site: (i) global front view and (ii) close-up view. Scale bars, 40 and 10 mm, respectively. (**E**) Sequence of events during payload dropping at a target location. Scale bar, 50 mm.

perching structure consisting of slender 1-mm-diameter rods (see fig. S12 for perching site design information). This new capability enabled various important features that were not possible with the old robot structure. In particular, energy conservation behaviors while perched were now possible during periods when the robot remained submerged. To unperch, the upgraded robot could effortlessly lift off from the perching structure by first turning on the current for 60 s, causing the hooks to open, and subsequently engaging fin flapping at 1 Hz to propel its body away from the perch (see Fig. 5D and movie S7).

Application: Payload carrier

The hook-like actuator could also be used to carry and deploy payloads. The opening of the hook whiskers can be seen in movie S8. Figure 5E shows snapshots from movie S9 where the upgraded robot carried a 2.5-g payload, nestled between the two hook whiskers, and subsequently released it at a designated location demarked by a blue ring. The robot reached the location, flapping at a frequency of 1 Hz. Subsequently, heating was initiated for the release of the payload. The hooks could support loads up to 7.5 g, equivalent to roughly 2.1% of the batoid's body weight. Future works will explore diverse actuation mechanisms, aiming to enhance the payload type and bearing capacity.

Passive thermal sensing and sample collection

The robot's multifunctionality was further enhanced by equipping it with thermochromic whiskers, enabling a visual representation of environmental temperature variations beyond 31°C. As shown in Fig. 6A and movie S10, the color of the whiskers changed within seconds from a red color in cold water (20°C) under an ice slab to a green tone when the upgraded robot entered a warm water region (38°C).

Beyond serving as thermal indicator, the passive whisker array shaped as a brush could also be used for sample collection. As shown in Fig. 6B and movie S11, the upgraded robot easily collected a specimen of bladderwort (*Utricularia gibba* L.) placed along its trajectory inside the water tank. The sample collection did not require complex controls, highlighting the versatility and potential of the passive whisker array for environmental studies. iFL3DP enabled

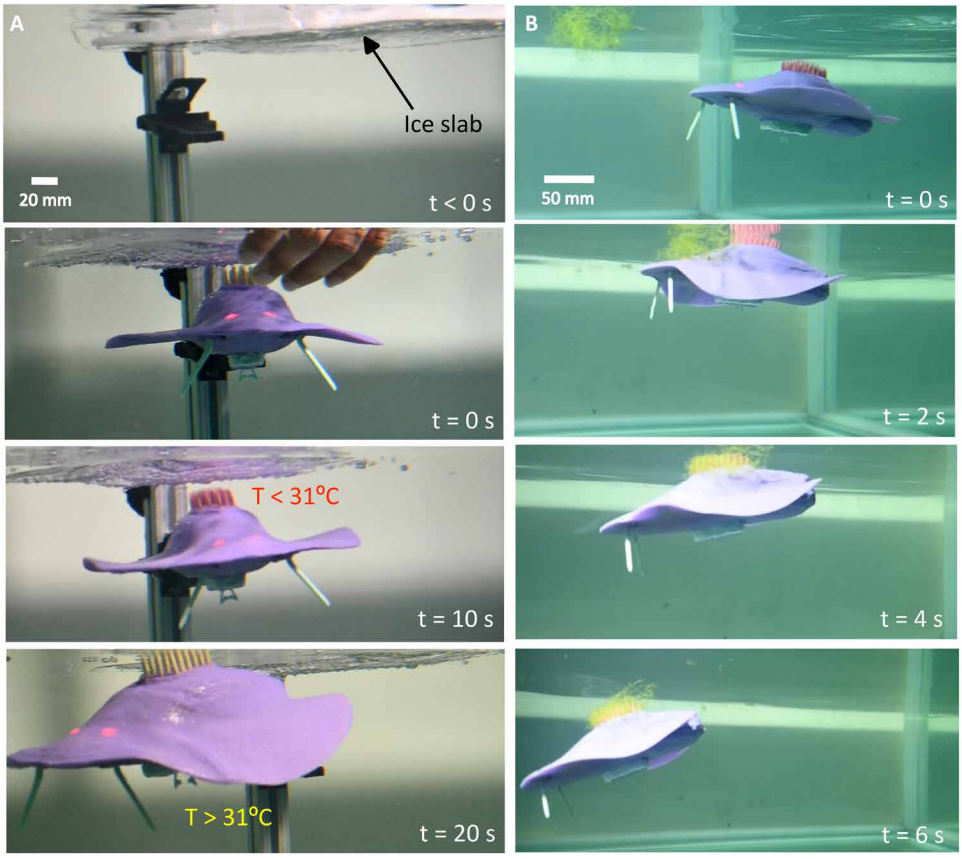

Fig. 6. Applications of the passive whisker array. (**A**) Temperature indication through visual feedback: A slab of ice was placed in water, under which the batoid was held for about 10 s, turning the thermochromic whiskers red. The whiskers turned back to a green color when the batoid moved into warm water. Scale bar, 20 mm. (**B**) Sequence of events during bladderwort sample collection. Scale bar, 50 mm.

easy customization of the bristled array depending on the desired application as well as a smooth integration of the new features along curved surfaces, preventing undesired casting, adhesive, or parting lines that could lead to unwanted flow separation when the vehicle maneuvers.

Robot repairs using iFL3DP

During its operational life span, the batoid robot could endure various forms of wear and tear, ranging from skin tears and whisker damage to diminished strain gauge sensitivity or potential leaks, as listed in Fig. 7. Peel tests and plucking tests were conducted to assess the resistance of the new components grafted on the robot's skin using iFL3DP. Interfacial toughnesses above 1.0 kJ m^{-2} were measured by conducting peel test experiments between fresh layers of silicone grafted on cured silicone layers (see fig. S4). These values, well above tendon and bone examples (~0.8 kJ m^{-2}) (*49*), showed a strong resistance to tear. In addition, plucking forces of ~14 N were measured for 4-mm-diameter whiskers, showing a strong adhesion (see fig. S13 for more details).

The use of RTV silicones to integrate new devices led to high robustness to damage. Despite this robustness, addressing hardware damage efficiently is still paramount to extend a robot's operational longevity and to minimize its environmental footprint. Here, iFL3DP provided an integrated platform for on-the-spot robot repairs, whereas alternative repair processes such as casting are limited to simple geometries. The iFL3DP robot repair workflow is illustrated in Fig. 7. Various damages that can occur to the batoid robot are depicted in Fig. 7A. Although the specific repair approach may vary depending on the type of damage, three general steps were typically involved: inspection and damage removal, reprinting with iFL3DP, and postprinting cleanup. Two real-life repair scenarios encountered in this study illustrated the efficacy of this workflow.

As shown in Fig. 7B, the first scenario consisted of the replacement of a deteriorated whisker (for example, severed or discolored) on the dorsal array. The faulty whisker along with its base was excised, resulting in a 4-mm–sided square cavity that was 2 mm deep. A graft layer was first printed to cover the cavity. Subsequently, a support bath was deposited to form a 7 mm–by–7 mm square base with a height of 12 mm, enabling the extrusion of a new thermochromic whisker using iFL3DP.

The second scenario shown in Fig. 7C addressed a malfunctioning tactile whisker. In this case, the whisker was removed with its strain gauge and graft layer, creating a vacant 12 mm–by–12 mm patch on the robot's skin. A new graft layer and strain gauge were printed on the vacant patch, followed by the deposition of a support bath, covering an area of 50 mm–by–30 mm with a height of 50 mm. Last, a tactile whisker was printed, and the support bath was washed off after the materials were cured.

Application of iFL3DP to other soft robots

Beyond soft robots for underwater applications and silicone-based soft robots, iFL3DP was also applicable to a broad range of soft robots, from pneunet actuators to crawling robots and even soft robots based on different materials such as textiles. The main applicability condition was to use materials that are both processable by iFL3DP and compatible with the robot surfaces. Broadly, five categories of materials commonly used in soft robots could be distinguished, all compatible with iFL3DP a priori: RTV silicone rubbers, ultraviolet (UV) curable resins, fabrics or textiles, thermoplastic polyurethanes (TPUs) or thermoplastic elastomers, and hydrogels.

A few examples of using iFL3DP on other robots were developed as proof of concept and are reported in Fig. 8 and movie S13 to illustrate the versatility of the method. First, a slant whisker array was printed on a fabric glove to demonstrate the feasibility of adding features to textile-based robotic components. Then, a whisker sensor was printed on a rubber caterpillar toy, and nail-like appendages were printed on a TPU pneunet. Last, a pneumatic finger was repaired by printing a silicone membrane on its surface. More information related to these applications is provided in the

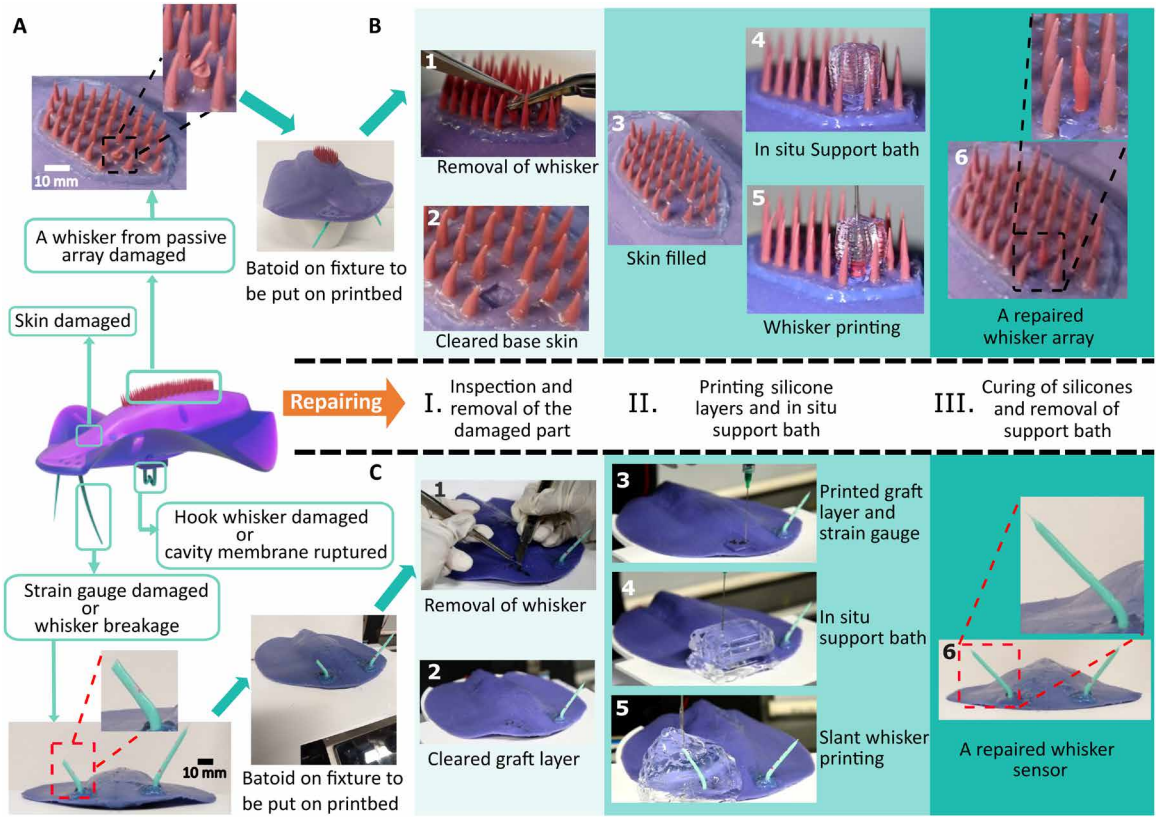

Fig. 7. Repairing a robot using iFL3DP. (**A**) Illustration of different types of damages that could occur on the batoid robot: the tearing of the skin, a faulty thermochromic whisker, a rupture of the cavity membrane or the damage of a hook in the actuator, or a faulty strain gauge or the breakage of a whisker from sensor. Scale bars, 10 mm. (**B** and **C**) Illustration of the six steps required for repairing the faulty thermochromic whisker and the damaged whisker sensor, respectively.

"Applicability of iFL3DP to other soft robots" section of Supplementary Text.

DISCUSSION

In this study, an AM approach, iFL3DP, was introduced. This approach facilitated the manufacture of multimaterial functional components directly on a preexisting soft robot and in situ repairs without the physical limitations associated with traditional AM processes, especially by substantially reducing required working spaces and postprocessing time. A comparison of trade-offs between various free-form fabrication technologies and iFL3DP is reported in table S6, showing advantages in terms of design free-form, multimaterial capabilities, space requirements, and postprocessing times. By comparison, jetting-based methods and vat polymerization offer higher resolutions with instant curing but a material library restricted to UV curable polymers and longer postprocessing times. However, the more recent vision-controlled jetting method substantially improved the multimaterial capabilities of these technologies with greater automation enabled by vision control (*50*).

The advantages of this method were demonstrated through the upgrade of an existing bioinspired swimming robot, in which three new components were seamlessly added despite challenging multimaterial structures: tactile sensing, hook-like actuators, and a thermal sensing array. These components presented highly complex geometries involving multiple materials (elastomers, conductive ink, and wires) that are challenging to fabricate using traditional manufacturing approaches used in soft robotics, such as casting and molding. In addition, the repair capabilities afforded by iFL3DP can prolong a robot's life span, underscoring its importance for sustainable efforts in soft and hybrid robotics. Overall, iFL3DP is a versatile and integrated fabrication approach that has the potential to reach one-step fabrication and maintenance of soft robots (*51*).

The components developed in this work underscored the manufacturing capabilities of iFL3DP. Further developments could be explored in future works to improve the performance of these components. For example, implementing machine learning and enhancing onboard computational capabilities is required to improve the robot's autonomous reaction to obstacles and bathymetry during free swimming (*52*, *53*). In addition, a thermal actuation mechanism was used for the hook-like actuator, but other mechanisms can be explored to provide faster response times and larger payload capacities.

Considering the underwater applications explored in this work, using iFL3DP directly underwater would be an exciting possibility. Preliminary experiments, reported in fig. S15, demonstrate the possibility of depositing silicone and support hydrogels underwater, thus enabling the fabrication of whiskers or other features. However, further research beyond the scope of this work is required to investigate the scope and influence of iFL3DP on printed structures in liquid environments.

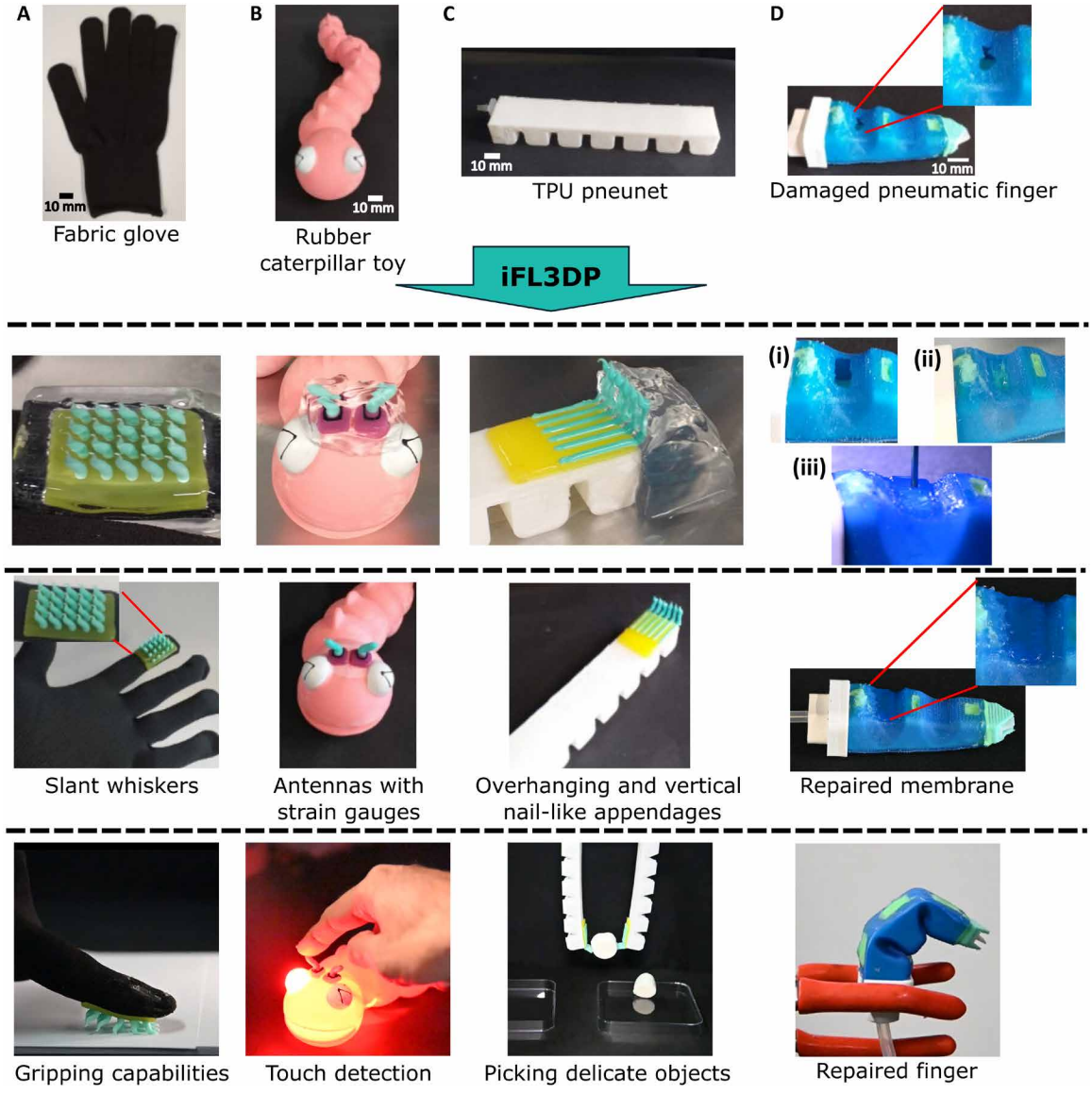

Fig. 8. Examples showing the applicability of iFL3DP on different types of robot materials and structures. (**A**) An array of slant whiskers was printed inside the support bath on a fabric glove, enabling easy flipping of paper sheets. (**B**) Two antennas along with strain gauges were added to the curved surface of a soft caterpillar, enabling touch detection with light-emitting diode lighting using a Bluno Nano microcontroller. (**C**) Overhanging and vertical nail-like appendages were printed on a pneunet made of TPU, enabling grasping of delicate objects such as marshmallows. (**D**) Repairs were conducted on a ruptured membrane of a pneumatic finger: (i) The ruptured membrane was trimmed to access the cavity beneath; (ii) the cavity was filled with support bath; and (iii) the membrane was printed on the surface of the printed support. The finger could bend again upon application of negative pressure. Scale bars, 10 mm [(A) to (D)].

Last, iFL3DP expands AM capabilities and can be seamlessly applied on a wide range of soft robots or object surfaces without requiring extensive effort in designing molds and engineering casting steps for each and every robot. However, resolutions reachable by iFL3DP techniques are limited by the ink stability inside the support, through a mechanism similar to Rayleigh-Plateau instability (*54*). As detailed in (*54*), a minimum stable feature size, l_C, can be estimated from the interfacial tension γ between the support material and the ink and the support's yield stress σ_y through the following relationship: $l_C = \gamma / \sigma_y$. For features smaller than l_C, the interfacial tension between the support and the inks leads to breakup of printed structures. In a previous work where elastomeric shells were printed inside vegetable oil–based supports, resolutions up to 300 μm were observed (*41*). For elastomeric inks printed inside Laponite-based supports, resolutions of ~100 μm were observed in the present work (see also fig. S8 for more information). To increase the resolution, other techniques, such as light-based AM techniques, could be considered to separately fabricate components before assembly on the robot. In addition, existing AM hardware and software still involve several labor-intensive processes, such as careful robot positioning, complex G-code generation in the case of uneven surfaces, and materials preparation. Enhancing hardware

capabilities with computer vision, laser-based scanners, and advanced slicing software will improve automation, notably via better assessment of the surface topologies and adjustment of printing parameters accordingly. These advances will further streamline the integration of iFL3DP into soft robot production workflows.

MATERIALS AND METHODS

Robot's design

The batoid robot was made of two main components: a thermoplastic shell that houses all the required electronics and actuation and an elastomeric skin (Ecoflex 00-30, Smooth-On) with two enlarged pectoral fins actuated by two lepidotrichia-inspired flappers. The electronics comprised a Li power source [903450 lithium polymer battery (3.7 V, 1500 mA hour), UNICELL, Singapore], a Bluno Nano board that has an ATmega328 microcontroller, and a Bluetooth low energy chip (TI CC2540) that facilitated wireless programming and data transmission through low-power Bluetooth 4.0 technology. The shell and flappers were 3D printed in acrylonitrile styrene acrylate (ASA). More information on the robot internal components is given in fig. S1.

Materials

Ecoflex 00-30, Smooth-Sil 960, SLO-JO, THI-VEX, silicone thinner, and Silc Pig pigments were purchased from Smooth-On Inc. The conductive grease (846 carbon conductive grease) was purchased from MG Chemicals, Canada. Laponite XLG was purchased from BYK Chemicals, Germany. Thermochromic pigment was obtained from Hali Industrial Co. Ltd., China. The pigment used was a double-color thermochromic pigment that changed from red to green at a transition temperature of 31°C.

Laponite bath

The support hydrogel was prepared by adding 5 wt % Laponite XLG to deionized water (18.2 megohms cm) and stirring the mixture at 60°C for 2 hours. After a setting time of 24 hours, the bath was transferred to 30-cm^3 syringes and mixed in a planetary mixer (ARE-310, THINKY) for 2 min at 2000 rpm, followed by defoaming for 2 min at 2200 rpm.

Rheological characterization

The rheological properties of the inks and support hydrogels were characterized using a controlled stress rheometer (Discovery HR-2 hybrid rheometer, TA Instruments). A 40-mm parallel plate geometry was used with a gap set to 100 μm. The viscoelastic region of the support was first checked via a frequency sweep conducted from 0.01 to 300 radians s^{-1}. The flow ramp measurements for studying the shear thinning behavior were carried out at a frequency of 1 Hz within the stress range of 0.01 to 2000 Pa at 25°C under a closed-loop temperature control for 60 s. The oscillatory stress sweeps of samples in the linear viscoelastic region were performed in the range of 0.1 to 2000 radians s^{-1} with a frequency of 1 Hz to measure G' and G''.

3D printing platform

Printing was conducted on a modified 3D printer (System 30M, Hyrel Inc.), which provided a multipurpose three-axis motion system. The fluid extrusion was carried out using a pneumatic fluid dispensing system (Ultimus V, Nordson EFD; Westlake, OH), with disposable 30-ml Luer-tipped syringes attached to the 3D printer with a custom-made adapter. The robot was fixed on the printer bed with a custom-made fixture 3D printed in ASA shown in fig. S16. G-code to deposit the support hydrogel and to print the functional components was generated using Python codes. To adapt to the robot's surface, G-code was generated on the basis of geometry from the robot computer-aided design files.

Robot's skin formulation

The skin was made of Ecoflex 00-30, prepared by mixing part A and part B in a 1:1 ratio. Part B was modified beforehand with 1 wt % of the curing retardant SLO-JO. After manual premixing, the mixture was further modified by adding 1 wt % of silicone thinner. The purple color was obtained by mixing 0.025, 0.05, and 0.01 wt % of Silc Pig red, blue, and white pigments, respectively. The mixture was mixed in a planetary mixer (ARE-500, THINKY) for 2 min at 1000 rpm followed by defoaming for 1 min at 2000 rpm. The mixture was poured into a 3D-printed mold (ASA) to form the skin around the shells and the flappers. After curing for 24 hours at room temperature, the robot was unmolded.

Tactile whisker sensor formulation and printing

The graft layer was prepared in a similar way to the skin, using Ecoflex 00-30. The SLO-JO quantity was increased to 4 wt % of part B, and the thickener THI-VEX was added to the mixture (4 wt % of part A). The mixture was loaded in a Luer lock-tip syringe (30 cm^3) and mixed in a planetary mixer (ARE-310, THINKY) for 2 min at 2000 rpm, followed by defoaming for 1 min at 2200 rpm. The graft layer was printed using a 20-gauge (G) needle (inner diameter of 0.66 mm, length of 50 mm) at 275 kPa and 5 mm s^{-1}.

The conductive carbon grease was loaded in a Luer lock-tip syringe (30 cm^3), mixed in a planetary mixer (ARE-310, THINKY) for 2 min at 2000 rpm, and defoamed for 1 min at 2200 rpm. The strain gauges were printed using a stainless steel 21-G needle (inner diameter of 0.60 mm, length of 50 mm) at 500 kPa and 0.8 mm s^{-1}.

The ink for the slant tactile whiskers was prepared from SS960, by mixing part A and part B in a 10:1 weight ratio modified with THI-VEX (0.05 wt % of part A). The mixture was mixed in a planetary mixer (ARE-310, THINKY) for 30 s at 2000 rpm, and then defoamed for 90 s at 2200 rpm and transferred into a Luer lock-tip syringe (30 cm^3). The whisker sensors were printed using a stainless steel 16-G needle (inner diameter of 1.3 mm, length of 50 mm) at 520 kPa.

A 3-mm vertical section was first printed at 0.67 mm s^{-1}, resulting in an overextruded thicker base that better transferred the mechanical stimuli to the strain gauges. A 40-mm-long slanted section was then printed with a 30° angle from the vertical at 0.8 mm s^{-1}.

Hook-like whisker actuator formulation and printing

The ink used for the cavity walls was prepared from SS960 by mixing part A and part B in a 10:1 weight ratio, modified with THI-VEX (1 wt % of part A), in a planetary mixer (ARE-310, THINKY) for 30 s at 2000 rpm, followed by defoaming for 90 s at 2200 rpm. The ink was then transferred into a Luer lock-tip syringe (30 cm^3). The walls were printed using a stainless steel 14-G needle (inner diameter of 1.7 mm, length of 50 mm) at 480 kPa and 2.5 mm s^{-1}.

The EF30 membrane was prepared by mixing part A and part B in a 1:1 weight ratio, modified with SLO-JO (4 wt % of part B); THI-VEX (4 wt % of part A); and a mixture of red, blue, and white Silc

Pig pigments (0.25 wt % of total weight in a 1:2:4 ratio). The mixture was loaded in a 30-cm^3 syringe and mixed in a planetary mixer (ARE-310, THINKY) for 2 min at 2000 rpm, followed by defoaming for 1 min at 2200 rpm. The membrane was printed using a stainless steel 20-G needle (inner diameter of 0.66 mm, length of 50 mm) at 275 kPa and 5 mm s^{-1}.

The ink for the hook-like whiskers was prepared with the same proportions as for the tactile whisker sensors. The hook-like whiskers were printed using a stainless steel 19-G needle (inner diameter of 0.8 mm, length of 50 mm) at 620 kPa. A 4-mm height was first extruded at 0.67 mm s^{-1} to create a thick base, followed by a vertical extrusion of 8 mm at 1 mm s^{-1}, and finished by an extrusion diagonally downward over 6 mm to form the hook.

Passive whisker array formulation and printing

The graft layer was prepared in a similar way to that for the graft layer used for the tactile whisker sensors. The graft layer was printed using a stainless steel 12-G needle (inner diameter of 2.3 mm, length of 50 mm) at 82 kPa and 8.3 mm s^{-1}.

The ink for the thermochromic whiskers was prepared from SS960 by mixing part A and part B in a 10:1 weight ratio, modified with SLO-JO (50 wt % part B), THI-VEX (0.05 wt % part A), and thermochromic pigment (5 wt % part A). The mixture was then mixed in a planetary mixer (ARE-310, THINKY) for 30 s at 2000 rpm, followed by defoaming for 90 s at 2200 rpm. The ink was then transferred into a syringe (30 cm^3), and the whiskers were printed using a stainless steel 20-G needle (inner diameter of 0.66 mm, length of 38 mm) at 620 kPa. The whiskers were 9 mm in height with a 2-mm-long initial section printed at 0.5 mm s^{-1}, followed by a vertical extrusion at 0.67 mm s^{-1} for 7 mm.

Algorithm for obstacle detection

The algorithm to detect peaks or spikes in a signal is based on statistical dispersion in the data points. If a new data point is at a distance greater than a preset threshold value multiplied by the SD from the moving mean of the signal, then the algorithm identifies the data point as a peak (*46*). For example, if the set threshold value is 3, then a data point that is further away than three times the SD from the moving mean will be flagged as a peak. An Arduino library (*55*) built on this algorithm was used to detect the peak in the whisker sensor data, caused by an encounter of the whisker with an obstacle.

Simulation

Simulations for the hook-like whisker actuator were conducted using Abaqus (Dassault Systèmes). A chamber with internal dimensions of 10 mm by 7 mm by 5 mm was modeled as an enclosed 3D deformable solid delimited by walls of 2-mm thickness. The internal fluid was modeled using a fluid cavity inside the chamber. The liquid was modeled to mimic ethanol properties, with a fluid density of 0.789 g ml^{-1} and a coefficient of volumetric thermal expansion of 0.0011°C^{-1}. The cavity walls and the two whiskers atop the soft membrane were modeled as 3D deformable solids, and a neo-Hookean model was used to model the hyperelastic properties of the elastomers: SS960 (C_{10} = 1782, D_1 = 0, density of 1.25 in SI units) was used for the side walls, the bottom membrane, and the whiskers; EF30 (C_{10} = 93, D_1 = 0, density of 1.07 in SI units) was used for the top soft membrane. The simulation was conducted by changing the temperature of the internal fluid, defined as a boundary condition, from 25° to 90°C. Mesh elements C3D8RH were used for the entire model.

Statistical analysis

In Fig. 3B and fig. S9 (B to D), data were recorded over 25, 30, or 100 cycles. Averages and SDs were calculated over the respective total number of cycles, with error bars representing the SDs. In Figs. 2 (F and G) and 5B and figs. S4 (D and E), S9A, and S13I, averages and SDs were calculated from three or four runs conducted, with the error bars representing the SDs.

In Figs. 3 (C and D) and 4 (C and E) and figs. S4F, S7 (A to D and F), S8 (A to C), S9 (E to H), S10 (A to D), S11A, and S13H, the presented data comprise single runs. These plots served as a platform to discuss the physical interpretation or sequence of events during the respective runs.

Supplementary Materials

The PDF file includes:

Supplementary Text
Figs. S1 to S16
Tables S1 to S6
Reference (*56*)

Other Supplementary Material for this manuscript includes the following:

Movies S1 to S13

REFERENCES AND NOTES

1. G. M. Whitesides, Soft robotics. *Angew. Chem. Int. Ed. Engl.* **57**, 4258–4273 (2018).
2. G.-Z. Yang, J. Bellingham, P. E. Dupont, P. Fischer, L. Floridi, R. Full, N. Jacobstein, V. Kumar, M. McNutt, R. Merrifield, B. J. Nelson, B. Scassellati, M. Taddeo, R. Taylor, M. Veloso, Z. L. Wang, R. Wood, The grand challenges of *Science Robotics*. *Sci. Robot.* **3**, eaar7650 (2018).
3. M. Sitti, Miniature soft robots—Road to the clinic. *Nat. Rev. Mater.* **3**, 74–75 (2018).
4. J. Xiong, J. Chen, P. S. Lee, Functional fibers and fabrics for soft robotics, wearables, and human–robot interface. *Adv. Mater.* **33**, e2002640 (2021).
5. C. Christianson, N. N. Goldberg, D. D. Deheyn, S. Cai, M. T. Tolley, Translucent soft robots driven by frameless fluid electrode dielectric elastomer actuators. *Sci. Robot.* **3**, eaat1893 (2018).
6. G. Li, X. Chen, F. Zhou, Y. Liang, Y. Xiao, X. Cao, Z. Zhang, M. Zhang, B. Wu, S. Yin, Y. Xu, H. Fan, Z. Chen, W. Song, W. Yang, B. Pan, J. Hou, W. Zou, S. He, X. Yang, G. Mao, Z. Jia, H. Zhou, T. Li, S. Qu, Z. Xu, Z. Huang, Y. Luo, T. Xie, J. Gu, S. Zhu, W. Yang, Self-powered soft robot in the Mariana Trench. *Nature* **591**, 66–71 (2021).
7. R. K. Katzschmann, J. DelPreto, R. MacCurdy, D. Rus, Exploration of underwater life with an acoustically controlled soft robotic fish. *Sci. Robot.* **3**, eaar3449 (2018).
8. G. Chowdhary, M. Gazzola, G. Krishnan, C. Soman, S. Lovell, Soft robotics as an enabling technology for agroforestry practice and research. *Sustainability* **11**, 6751 (2019).
9. K. C. Galloway, K. P. Becker, B. Phillips, J. Kirby, S. Licht, D. Tchernov, R. J. Wood, D. F. Gruber, Soft robotic grippers for biological sampling on deep reefs. *Soft Robot.* **3**, 23–33 (2016).
10. S. Jain, S. Dontu, J. E. M. Teoh, P. V. Y. Alvarado, A multimodal, reconfigurable workspace soft gripper for advanced grasping tasks. *Soft Robot.* **10**, 527–544 (2023).
11. B. Mazzolai, C. Laschi, A vision for future bioinspired and biohybrid robots. *Sci. Robot.* **5**, eaba6893 (2020).
12. F. Hartmann, M. Baumgartner, M. Kaltenbrunner, Becoming sustainable, the new frontier in soft robotics. *Adv. Mater.* **33**, e2004413 (2021).
13. M. Baumgartner, F. Hartmann, M. Drack, D. Preninger, D. Wirthl, R. Gerstmayr, L. Lehner, G. Mao, R. Pruckner, S. Demchyshyn, L. Reiter, M. Strobel, T. Stockinger, D. Schiller, S. Kimeswenger, F. Greibich, G. Buchberger, E. Bradt, S. Hild, S. Bauer, M. Kaltenbrunner, Resilient yet entirely degradable gelatin-based biogels for soft robots and electronics. *Nat. Mater.* **19**, 1102–1109 (2020).
14. A. A. La Mattina, S. Mariani, G. Barillaro, Bioresorbable materials on the rise: From electronic components and physical sensors to in vivo monitoring systems. *Adv. Sci.* **7**, 1902872 (2020).

15. A. Heiden, D. Preninger, L. Lehner, M. Baumgartner, M. Drack, E. Woritzka, D. Schiller, R. Gerstmayr, F. Hartmann, M. Kaltenbrunner, 3D printing of resilient biogels for omnidirectional and exteroceptive soft actuators. *Sci. Robot.* **7**, eabk2119 (2022).
16. A. M. Nguyen, A. Seibel, Recycling-oriented design in soft robotics. *Actuators* **8**, 62 (2019).
17. C. Tang, B. Du, S. Jiang, Q. Shao, X. Dong, X.-J. Liu, H. Zhao, A pipeline inspection robot for navigating tubular environments in the sub-centimeter scale. *Sci. Robot.* **7**, eabm8597 (2022).
18. Y. Lin, Y.-X. Xu, J.-Y. Juang, Single-actuator soft robot for in-pipe crawling. *Soft Robot.* **10**, 174–186 (2023).
19. N. Boddeti, T. Van Truong, V. S. Joseph, T. Stalin, T. Calais, S. Y. Lee, M. L. Dunn, P. V. y Alvarado, Optimal soft composites for under-actuated soft robots. *Adv. Mater. Technol.* **6**, 2100361 (2021).
20. X. Ji, X. Liu, V. Cacucciolo, M. Imboden, Y. Civet, A. El Haitami, S. Cantin, Y. Perriard, H. Shea, An autonomous untethered fast soft robotic insect driven by low-voltage dielectric elastomer actuators. *Sci. Robot.* **4**, eaaz6451 (2019).
21. D. Rus, M. T. Tolley, Design, fabrication and control of soft robots. *Nature* **521**, 467–475 (2015).
22. T. G. Thuruthel, B. Shih, C. Laschi, M. T. Tolley, Soft robot perception using embedded soft sensors and recurrent neural networks. *Sci. Robot.* **4**, eaav1488 (2019).
23. C. D. Onal, D. Rus, A modular approach to soft robots, in *2012 4th IEEE RAS & EMBS International Conference on Biomedical Robotics and Biomechatronics (BioRob)* (IEEE, 2012), pp. 1038–1045.
24. C. Zhang, P. Zhu, Y. Lin, Z. Jiao, J. Zou, Modular soft robotics: Modular units, connection mechanisms, and applications. *Adv. Intell. Syst.* **2**, 1900166 (2020).
25. E. Roels, S. Terryn, F. Iida, A. W. Bosman, S. Norvez, F. Clemens, G. Van Assche, B. Vanderborght, J. Brancart, Processing of self-healing polymers for soft robotics. *Adv. Mater.* **34**, e2104798 (2022).
26. R. Das, S. P. M. Babu, F. Visentin, S. Palagi, B. Mazzolai, An earthworm-like modular soft robot for locomotion in multi-terrain environments. *Sci. Rep.* **13**, 1571 (2023).
27. A. J. Partridge, H.-Y. Chen, N. H. Le, C. Xu, H. Eichorn, E. Pulvirenti, A. Manzini, A. T. Conn, J. Rossiter, ReRobot: Recycled materials for trustworthy soft robots, in *2022 IEEE 5th International Conference on Soft Robotics (RoboSoft)* (IEEE, 2022), pp. 148–153.
28. O. Pialot, D. Millet, Why the upgradability is a present-day opportunity for designing sustainable systems? *Procedia CIRP* **48**, 96–101 (2016).
29. M. Inoue, S. Yamada, T. Yamada, S. Bracke, Product upgradability for satisfying future performance, low price and environmental loads, and manufacturer profitability throughout the product lifecycle. *Procedia CIRP* **48**, 40–44 (2016).
30. M. A. Khan, S. Mittal, S. West, T. Wuest, Review on upgradability—A product lifetime extension strategy in the context of product service systems. *J. Clean. Prod.* **204**, 1154–1168 (2018).
31. S. Ford, M. Despeisse, Additive manufacturing and sustainability: An exploratory study of the advantages and challenges. *J. Clean. Prod.* **137**, 1573–1587 (2016).
32. M. Gebler, A. J. M. Schoot Uiterkamp, C. Visser, A global sustainability perspective on 3D printing technologies. *Energy Policy* **74**, 158–167 (2014).
33. E. Delaney, W. Liu, Z. Zhu, Y. Xu, J. S. Dai, The investigation of environmental sustainability within product design: A critical review. *Des. Sci.* **8**, e15 (2022).
34. H. Le Ferrand, Toward sustainable 3D printing. *Acc. Mater. Res.* **1**, 123–125 (2020).
35. T. J. Wallin, J. Pikul, R. F. Shepherd, 3D printing of soft robotic systems. *Nat. Rev. Mater.* **3**, 84–100 (2018).
36. G. Stano, G. Percoco, Additive manufacturing aimed to soft robots fabrication: A review. *Extreme Mech. Lett.* **42**, 101079 (2021).
37. V. S. Joseph, T. Calais, T. Stalin, S. Jain, N. K. Thanigaivel, N. D. Sanandiya, P. V. y Alvarado, Silicone/epoxy hybrid resins with tunable mechanical and interfacial properties for additive manufacture of soft robots. *Appl. Mater. Today* **22**, 100979 (2021).
38. R. L. Truby, M. Wehner, A. K. Grosskopf, D. M. Vogt, S. G. M. Uzel, R. J. Wood, J. A. Lewis, Soft somatosensitive actuators via embedded 3D printing. *Adv. Mater.* **30**, e1706383 (2018).
39. E. Mirdamadi, N. Muselimyan, P. Koti, H. Asfour, N. Sarvazyan, Agarose slurry as a support medium for bioprinting and culturing freestanding cell-laden hydrogel constructs. *3D Print. Addit. Manuf.* **6**, 158–164 (2019).
40. T. Calais, N. D. Sanandiya, S. Jain, E. V. Kanhere, S. Kumar, R. C.-H. Yeow, P. Valdivia Y Alvarado, Freeform liquid 3D printing of soft functional components for soft robotics. *ACS Appl. Mater. Interfaces* **14**, 2301–2315 (2022).
41. T. Calais, A. Castillo Ugalde, A. C. A. Rong, P. V. y Alvarado, Freeform liquid 3D printing of hydraulically enhanced dielectric actuators. *Mater. Today Proc.* **70**, 83–89 (2022).
42. T. V. Truong, V. K. Viswanathan, V. S. Joseph, P. V. y Alvarado, Design and characterization of a fully autonomous under-actuated soft batoid-like robot, in *2019 IEEE/RSJ International Conference on Intelligent Robots and Systems (IROS)* (IEEE, 2019), pp. 5826–5831.
43. K. S. Sekar, M. Triantafyllou, P. V. y Alvarado, Flapping actuator inspired by lepidotrichia of ray-finned fishes, in *2014 IEEE/RSJ International Conference on Intelligent Robots and Systems* (IEEE, 2014), pp. 1120–1126.
44. T. Stalin, S. Jain, N. K. Thanigaivel, J. E. M. Teoh, A. R. P. Mathai, P. V. y Alvarado, Automated fiber embedding for soft mechatronic components. *IEEE Robot. Autom. Lett.* **6**, 4071–4078 (2021).
45. M. Sato, Preliminary report on the barbels of a Japanese goatfish, *Upeneoides bensasi* (Temminck & Schlegel). *Sci. Rep. Tohoku. Imp. Univ. 4th Ser. (Biol.)* **11**, 259–264 (1937).
46. J. P. G. van Brakel, Robust peak detection algorithm using z-scores (Stack Overflow, 2014); https://stackoverflow.com/questions/22583391/peak-signal-detection-in-realtime-timeseries-data/22640362#22640362.
47. S. J. Blott, K. Pye, Particle size scales and classification of sediment types based on particle size distributions: Review and recommended procedures. *Sedimentology* **59**, 2071–2096 (2012).
48. J. Wolfe, D. N. Hill, S. Pahlavan, P. J. Drew, D. Kleinfeld, D. E. Feldman, Texture coding in the rat whisker system: Slip-stick versus differential resonance. *PLOS Biol.* **6**, e215 (2008).
49. J. D. Bobyn, G. J. Wilson, D. C. MacGregor, R. M. Pilliar, G. C. Weatherly, Effect of pore size on the peel strength of attachment of fibrous tissue to porous-surfaced implants. *J. Biomed. Mater. Res.* **16**, 571–584 (1982).
50. T. J. K. Buchner, S. Rogler, S. Weirich, Y. Armati, B. G. Cangan, J. Ramos, S. T. Twiddy, D. M. Marini, A. Weber, D. Chen, G. Ellson, J. Jacob, W. Zengerle, D. Katalichenko, C. Keny, W. Matusik, R. K. Katzschmann, Vision-controlled jetting for composite systems and robots. *Nature* **623**, 522–530 (2023).
51. E. Sachyani Keneth, A. Kamyshny, M. Totaro, L. Beccai, S. Magdassi, 3D printing materials for soft robotics. *Adv. Mater.* **33**, 2003387 (2021).
52. D. Kim, S.-H. Kim, T. Kim, B. B. Kang, M. Lee, W. Park, S. Ku, D. Kim, J. Kwon, H. Lee, J. Bae, Y.-L. Park, K.-J. Cho, S. Jo, Review of machine learning methods in soft robotics. *PLOS ONE* **16**, e0246102 (2021).
53. B. W. K. Ang, C.-H. Yeow, A learning-based approach to sensorize soft robots. *Soft Robot.* **9**, 1144–1153 (2022).
54. C. S. O'Bryan, T. Bhattacharjee, S. R. Niemi, S. Balachandar, N. Baldwin, S. T. Ellison, C. R. Taylor, W. G. Sawyer, T. E. Angelini, Three-dimensional printing with sacrificial materials for soft matter manufacturing. *MRS Bull.* **42**, 571–577 (2017).
55. C. Leandro, Peak detection (Real time peak detection with z-score for Arduino), https://github.com/leandcesar/PeakDetection.
56. L. F. Kawashita, D. R. Moore, J. G. Williams, Protocols for the measurement of adhesive fracture toughness by peel tests. *J. Adhes.* **82**, 973–995 (2006).

Acknowledgments: We thank N. K. Thanigaivel (Singapore University of Technology and Design) for providing the rubber caterpillar toy and the TPU pneunet prototype. **Funding:** This research project was supported by A*STAR under its Science and Engineering Research Council (SERC) award W2025d0243 and by the National Research Foundation, Prime Minister's Office, Singapore under its Campus of Research Excellence and Technological Enterprise (CREATE) programme. **Author contributions:** E.K. worked on concept ideation, electronics of sensor-actuator and data storage, fabrication, coding, all the characterization and application experiments, and manuscript writing and reviewing. T.C. worked on concept ideation, simulation, rheological characterization, and manuscript writing and reviewing. S.J. worked on the design of the printed circuit board for control and power systems. A.R.P.M. worked on the electronics of the control and power systems. A.C. worked on application experiments and drawing figures and cover illustration. T.S. worked on the casting of the batoid robot and characterization of the whisker printing. V.S.J. worked on peel tests and pluck tests. P.V.y.A. secured funds and worked on concept ideation and manuscript writing and reviewing. **Competing interests:** The authors declare that they have no competing interests. **Data and materials availability:** All data needed to evaluate the conclusions in the paper are present in the paper or the Supplementary Materials. All data shown in the paper and relevant codes have been deposited on zenodo.org (DOI: 10.5281/zenodo.14016789).

Submitted 15 December 2023
Accepted 5 November 2024
Published 4 December 2024
10.1126/scirobotics.adn4542

Science Robotics

Upgrading and extending the life cycle of soft robots with in situ free-form liquid three-dimensional printing

Elgar Kanhere, Théo Calais, Snehal Jain, Aby Raj Plamootil Mathai, Aaron Chooi, Thileepan Stalin, Vincent Sebastian Joseph, and Pablo Valdivia y Alvarado

Sci. Robot. **9** (97), eadn4542. DOI: 10.1126/scirobotics.adn4542

Editor's summary

As the soft robotics field progresses, advancements in sensors and actuation, along with deterioration, can render earlier robot generations obsolete, reducing their usable life spans. To promote sustainability in soft robotics, Kanhere *et al.* developed an in situ free-form liquid three-dimensional printing strategy that enables upgrades and repairs to existing robots. A specially formulated gel was printed directly onto the robot's surface, which served as a support medium for the direct printing of new features onto various surfaces without the need for a special container. The technique was used to upgrade a batoid-like soft robot with tactile sensors, a passive whisker array, and actuated hooks, as well as to repair skin tears and whisker damage, thereby extending the robot's life span. —Melisa Yashinski